Engineering Science and Technology, an International Journal 39 (2023) 101342

HOSTED BY

Contents lists available at ScienceDirect

Engineering Science and Technology,
an International Journal

journal homepage: www.elsevier.com/locate/jestch

Effect of HVOF processing parameters on $Cr_3C_2 - NiCr$ hard coatings deposited on AISI 4140 steel

S. Sauceda [a,*], S. Lascano [a,**], J. Núñez [a], C. Parra [b], C. Arévalo [c], L. Béjar [d]

[a] Departamento de Ingeniería Mecánica, Universidad Técnica Federico Santa María, Avda. Vicuña Mackenna N° 3939, San Joaquín, Santiago, Chile
[b] Laboratorio de Nanobiomateriales, Departamento de Ingeniería Mecánica, Universidad técnica Federico Santa María, Avenida España 1680, Valparaíso, Chile
[c] Departamento de Ingeniería y Ciencia de los Materiales y del Transporte, E.T.S. de Ingeniería-Escuela Politécnica Superior, Universidad de Sevilla, Camino de los Descubrimientos, s/n, 41092 Seville, Spain
[d] Facultad de Ingeniería Mecánica, Universidad Michoacana de San Nicolás de Hidalgo, Ciudad Universitaria, Morelia 58000, Mexico

ARTICLE INFO

Article history:
Received 22 June 2022
Revised 7 November 2022
Accepted 17 January 2023

Keywords:
Thermal spray coating
HVOF
Experimental design
Hard coatings

ABSTRACT

High Velocity Oxygen Fuel (HVOF) thermal spray coating is a deposition process that is widely employed at present to improve surfaces and the remanufacturing of components subject to severe wear, offering an alternative to reduce the cost of spare parts and used as a substitute for electro-chromium, also generating greater thickness than chemical vapor deposition and physical vapor deposition. This study evaluates the influence of the projected application parameters for $Cr_3C_2 - 20(Ni20Cr)$ coatings on AISI 4140 steel using the HVOF technique. To do so, a 2^4 factorial experimental design was used to evaluate the effect on the thickness, porosity, surface hardness, and microhardness in the cross-section, produced by four of the main operational factors in the HVOF process: the fuel/oxygen (F/O) ratio entering the combustion chamber, powder flow, the roughness of the substrate before deposition, and spray gun speed. The morphology of the $Cr_3C_2 - 20(Ni20Cr)$ powders and the microstructure of the coatings were studied through a scanning electron microscope and energy dispersive spectroscopy, while the composition were analyzed by X-ray diffraction. It was determined that: (i) the F/O ratio is the operation parameter with the most significant influence on the properties studied; (ii) the gun speed has a significant effect on the thickness generated and porosity; and (iii) the powder flow and roughness of the substrate have a greater effect on the surface hardness and microhardness. Finally, it was determined that coatings with great thickness, low porosity, and great hardness, ideal for the recovery of parts, can be achieved from a F/O ratio of 0.45 and a powder flow with the system feeder rotating at 12 rpm, applied to a substrate with a roughness of $R_a = 18$ µm, combined with a spray gun speed of 5 mm/s.

1. Introduction

There is currently an increasing trend towards products with shorter useful life and industrial waste which adds further complexity to the task of protecting the environment [1]. Surface engineering and additive manufacturing techniques can provide solutions aimed at reusing components with a substrate at a lower cost and reduced environmental impact, through the application of a coating with sufficient thickness and quality to recover the initial geometry lost due to severe wear and tear, which also helps reduce time, costs, and energy consumption, in comparison to the manufacturing of a new component [2,3].

There are different techniques to produce functional coatings that are resistant to wear and tear and corrosion, which can be applied to different shaped objects. In particular, the high velocity oxygen-fuel (HVOF) technique projects a powder at high supersonic speed generated by an increase in pressure from the combustion of kerosene and oxygen, adhering to the substrate through plastic deformation [4,5]. This process achieves highly adherent coatings, with low porosity ($< 2\%$), high microhardness ($> 800HV$) [6,7], good resistance to corrosion [8–10], and great thickness (> 200 µm) [11–14], which is why it is currently used in the industry to recover mechanical components such as tools, valves, turbine blades, axles, or decorative surfaces [15–19].

This technique is complex by nature and involves a large number of operating parameters that affect the formation of the coating, its microstructure, and mechanical properties. The effect of these parameters must be known in order to maximize thickness

---

* Corresponding author.
** Principal corresponding author.

E-mail addresses: sergio.sauceda@usm.cl (S. Sauceda), sheila.lascano@usm.cl (S. Lascano).

https://doi.org/10.1016/j.jestch.2023.101342
2215-0986/

[3,20,21], decrease the presence of porosity in the coating, and obtain an adequate adherence to the substrate and cohesion among the sprayed layers. This helps avoid nucleation and the development of cracks that compromise quality [22–24] and guarantees that the mechanical properties are preserved during the processing cycle and use of the component [25,26]. Increase surface hardness to avoid wear and tear [26–28].

The microhardness in the cross-section of the coating helps us to know the state of some mechanical properties, such as Young's modulus and Poisson's ratio, since they follow the same trend [29]. In addition, it is a technique that allows us to achieve the coating quality without the difficulties of large sample sizes required in conventional mechanical tests on cylindrical parts applied in the industry [30]. This justifies the study of processing parameter's effect on the coating quality using process mapping methodologies [31,32] and experimental design [33–35] to achieve an application protocol, control model, and process optimization.

The effect of the variables associated with HVOF application on the physical and mechanical properties of coatings has been studied in literature with different experimental designs; Clavijo et al. [36] studied the influence of the fuel/oxygen (F/O) ratio, gun spray distance, and powder feed rate (PFR), on the speed and temperature of the TiO_2 particles projected, using 2^3 factorial designs; the first to study the effect on the speed and temperature of the particles, and the second with the same parameters at different values for the study of splats formed on the coating surface. In addition to these three input variables, Khan et al. [37] also analyzed the effect of thickness in a 2^4 factorial design on properties such as microhardness, contact angle, and cross-section porosity in $WC-12Co$ coatings over AISI 4340 steel. In particular, the microhardness of the coating depends on the placement of splats and dispersion of phases in the coating, since a better distribution of splats and phases generates greater microhardness and better quality of the coating [38,39].

Meanwhile, J. Singh et al. [40] used Taguchi orthogonal factorial designs to study the behavior of coating wear and tear, for both $WC-10Co-4Cr$ and $Ni-20Cr_2O_3$ over SS304 steel. In the case of $Cr_3C_2-25(Ni20Cr)$ coatings, the optimization method has been studied by Varis et al. [41] to understand the behavior of the stoichiometry parameters in combustion on the fatigue of these coatings applied to S355J2G3 structural steel. The studies of this coating have been oriented to optimize its wear and fatigue resistance, proving that this material is suitable for high-wear applications. However, further studies on the optimization of manufacturing based on remanufacturing and component recovery capacity, evaluating the densification and thicknesses are essential to achieved industrial applications.

Nickel–chromium based coatings are widely used in the industry for the remanufacturing of components [3,42] thanks to the excellent resistance to corrosion, higher than that seen for tungsten carbide coatings [8,43], and their resistance to wear and tear exceeds that of electro-chromium. It is also possible to apply these to different types of steel. The wide acceptance of AISI 4140 steel makes it one of the most widely used steels. It uses in manufacturing rollers, turbines, and transmission shafts for the mining, energy, automotive, and oil industries [44,45].

However, despite numerous studies related to the properties of $Cr_3C_2-(NiCr)$ coatings over stainless [46–48] and low-carbon steels [7,22,38,49], there are no optimization studies by experimental design for nickel–chromium based coatings on this type of steel.

This study proposes to evaluate the effect of the process variables in the deposition of $Cr_3C_2-20(Ni20Cr)$ coatings over an AISI 4140 steel substrate using the HVOF technique. We aim to generate hard coatings with thicknesses over 100 µm, low porosity ($<2\%$), and high microhardness (>800 HV) to obtain dense and good-quality coatings that can be used for recovering components of cylindrical geometries with large dimensions, such as shafts, rods, piston rings, among others. For this, a 2^4 factorial design is proposed to evaluate the main effects and combined effects of the powder feed rate, gun speed, fuel/oxygen ratio, and roughness of the substrate on porosity, adherence, hardness, and final thickness.

2. Materials and methods

This study used $Cr_3C_2-20(Ni20Cr)$ powder with a size distribution of 45 ± 15 µm supplied by Sulzer Metco, USA (Woka 7102). The initial powder was characterized using Scanning Electron Microscopy (SEM), FEI QuantaTM 250 FEG SEM,equipped with energy-dispersive X-ray spectroscopy (EDS) for the analysis of local distribution and area of metallic and non-metallic elements in a powder particle. The images obtained from the powder surfaces were taken using 20 kV accelerating voltage. The phases found in the powder were obtained through X-ray Diffraction (XRD) using a STOE STADI MP diffractometer, a radiation of CuKα_1 ($\lambda = 0.15406$ nm), one step from 0.02°, and a permanence time ranging from 30°to 70°at 2θ.

2.1. Experimental design

This study used a 4-variable and two-level (2^4) factorial design, to evaluate the effect of each of the variables on (i) thickness, (ii) internal porosity, (iii) surface hardness, and (iv) microhardness in the cross-section of the coatings deposited. For this, the following variables were taken: the fuel/oxygen ratio (A), the powder flow rate (B), the roughness of the substrate before application of the coating (C), and gun speed (D). The two levels used, as well as the parameters that remained constant, are shown in Table 1. The fuel/oxygen ratio and flow rate were chosen thanks to their strong influence on quality, residual tension, and coating thickness [50,51]. Roughness, on the other hand, is closely related to coating adherence and the formation of splats of the projected particles [52], while the longitudinal gun speed was considered because the goal is to reduce coating application times without sacrificing quality, therefore this must be studied in order to propose an optimal level.

For all statistical analysis, the Statgraphics®Centurion XVIII software was used. A prediction model was prepared for each of the output variables using the linear first order equation, with interactions:

$$\hat{y} = \beta_0 x_i + \sum_{i=1}^{K} \beta_i x_i + \sum_{i>i}\sum_{i=1} \beta_{ii} x_i x_i + \epsilon \tag{1}$$

where $\hat{y}$ represents the output variable to be predicted, x_i represents the respective variable of each regression coefficient β obtained, and ϵ is a term of random error.

Table 1
Summary of the experimental design and results of HVOF coatings.

Variables	Level	
	Low (−1)	High (+1)
Fuel/oxygen ratio (F/O)	0.3	0.45
Powder flow $[rpm]$	12	20
Surface roughness Ra $[\mu m]$	18	28
Gun speed $[mm/s]$	5	15

2.2. Coating application conditions

The deposition was performed using a JET4L-100 liquid fuel HVOF spray gun. The deposition conditions were established through the experimental design with the levels shown in Table 1.

The F/O was obtained through the ratio:

$$F/O = \frac{Kerosene\ flow\ [ml/min]}{oxygen\ flow\ [l/min]} \tag{2}$$

In the case of powder flow, a Metallisation®model 2007MF-PF powder feeder was used. The powder was fed volumetrically using a disc with perforated holes around the circumference. An inverter controls the revolutions per minute (*rpm*) of the disc and a mass flow meter controls the gas carrier flow that transports the powder to the chamber. Both devices are connected to a programmable logical controller. For powder parameters, the powder flow regulation variable used was *rpm* of the feed disc such that, for a single gas carrier flow, a greater feed disc speed would generate a greater powder flow. It should be noted that for all applications, the powder used came from the same commercial container to avoid variability in the system.

Prior to the coating process, the surface was shot peened with a hardened grade 4 steel grit. Using a roughness tester PCE-RT 10, measurements were made at $0^\circ, 120^\circ$, and 240° around the circumference of the cylindrical tube to ensure homogeneous values.

Finally, the fourth variable is the longitudinal speed of the gun as it moves longitudinally through the lathe with the cylinder mounted.

In the applications, all other variables remained constant at the characteristic values recommended by the machine manufacturer, such as, gas carrier flow and spray distance, maintaining an initial substrate temperature of 50 °C, and projecting 10 layers at an angle of 90° to generate thicknesses of around 100 μm.

2.3. Microstructural characterization of the coatings

The powder was deposited over AISI 4140 steel cylinders with a diameter of 110 mm and 10 cm long. Samples of 1 cm^3 were obtained with a coated curved surface. This is due to the objective of manufacturing and remanufacturing curved surfaces found in shafts, rods, or pistons [53,54]. Due to the angle of impact of the particles of the deposited material, they behave differently when deposited on the substrate, affecting its final properties [55].

The coating cross-section surface was prepared for metallography analysis using a grinding and polishing sequence according to the ASTM E3-11 standard. The treated section was analyzed through the SEM using images of backscattered electrons (Circular Backscatter Detector, CBS) and an accelerating voltage of 20 kV to characterize the status of the coating and substrate and to obtain a better contrast between the phases present in the coating.

Micro X-ray Diffraction (μXRD) analysis was then performed on the coated section (surface and cross section) with a capillary of 1 mm, with the aim to study changes in coating composition after deposition. The μXRD patterns were obtained with a D8 DISCOVER diffractometer equipped with a 2D detector model VANTEC-500 (Bruker, Germany), using CuKα_1 radiation ($\lambda = 0.15406$ nm) and a step size of 20°; the scan was recorded in the 2θ range comprised from 20° to 60° and a time per step of 10 min, with tube conditions of 40 kV and 40 mA. Thus, three frames were collected, each frame being about 20 min. Each frame allows seeing a range of about 30° 2θ. After integrating the frames, diffractograms in the range 30° to 70° were obtained for analysis.

2.4. Characterization of thickness

To ensure a representative measurement of the coating thickness, 3 images were taken of different sections of each sample obtained in each experiment, using SEM images at 500x to determine the coating end edges. In each image, 3 different measurements were obtained, and measurement were repeated 3 times to take the average and calculate the standard deviation.

2.5. Characterization of porosity

To estimate the porosity, 3 SEM images at 1000x and 3 images at 2000x of each sample were used, taken from 3 different sections of the coating. The images of the sections were converted to binary format using the ImageJ®software [56], obtaining the percentage of totally black area in the coating section in relation to the total surface of the selected section, and this was defined as the porosity percentage. This process was repeated 3 times for each measurement, and all measurements of a sample were averaged to calculate the standard deviation. The defects were characterized qualitatively with the same images.

2.6. Characterization of surface hardness

To evaluate the surface hardness on the Rockwell C (HRC) scale, a Rockwell TH320 (Times, China) Durometer was used with a load of 150 kg for 10 s, according to the ASTM E18-17 standard, taking the total average of 6 indentations by sample linearly along a plane tangential to the coated curved surface. Based on the results, the effect on interface adhesion, density, thickness, and cohesion over the substrate-coating ensemble was studied indirectly.

2.7. Characterization of microhardness

Performing microhardness in the cross-section of the sample allows us to evaluate the intrinsic characteristics of the isolated coating, consisting of hard particles and the binder material. On the other hand, surface hardness evaluates coating-substrate assembly behavior indirectly by assessing adhesion, density, thickness, and cohesion [57]. When a spherical indenter is placed on the surface, the generated stress at the interface, if sufficient, can overcome adhesion resistance or cause damage due to low cohesion [58].

The microhardness in the cross-section of the coated samples was analyzed through a microindentation profile from the coating surface to the substrate, using a Vickers (MVK-HVL, Akashi) microdurometer with loads of 200 and 25 gf for F/O ratios of 0.45 and 0.3 respectively, with a 10 s maintenance time. This difference in load is because coatings with a F/O of 0.3 were not thick enough to perform indentations with a higher load. Three indentation profiles were prepared for each coating, obtaining the average measurements. Moreover, an indentation profile was prepared in the interface of the substrate coating with loadings of $50, 100, 200, 300, 500$ and 1000 gf to study adhesion, and this process was repeated 3 times for each sample. The distributions of micro-hardness were plotted using individual readings measured for the coating with the same interval along three parallel lines spaced (i.e. 0.5 mm) from one another which, as such, they will represent the averaged distribution of the micro-hardness of the coating, measured from surface layer of the coating up to substrate material.

3. Results and discussion

3.1. Characterization of the powder

The powders used present a spherical morphology and are composed of a subset of agglomerate particles, as observed in the CBS-SEM images (Fig. 1). The analysis performed using the compositional map (mapping) in Fig. 1d confirms the chemical composition of the powder and evidence the presence of Ni in the clear gray zone as an agglomerating phase in the irregular sections that join the C and Cr particles corresponding to chromium carbide, which are seen as dark gray zones.

The XRD obtained for the $CrC-20(Ni20Cr)$ powder used for the coatings is shown in Fig. 2. The diffraction peaks of Cr_3C_2 (space group symmetry Pnma (No. 62)) and Ni (space group symmetry Fm-3m (No. 225)) were the main phases identified. This is consistent with the compounds indicated by the manufacturer, and phases were found in a lower proportion such as in Cr_7C_3 (space group of PMCM (No. 51)) and $Cr_{23}C_6$ (space group symmetry Fm-3m (No. 225)), according to literature [49,6].

The summary of the properties evaluated (porosity, thickness, surface hardness, and microhardness) corresponding to the application performed in the 2^4 experimental design (16 samples), can be found in Table 2. In the case of thickness and porosity, both measured through SEM, their values vary between 20 and 274 μm and 1.4 and 33%, respectively, while the surface hardness and microhardness ranges from 14 to 43 HRC and 495 to 930 HV, respectively.

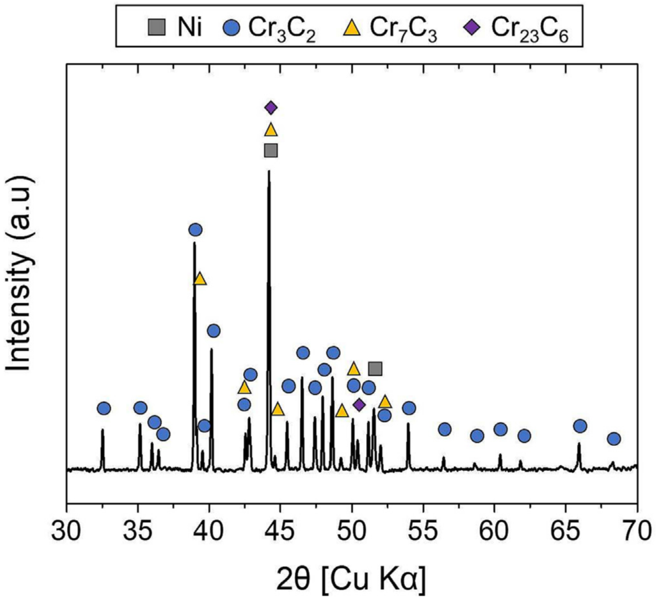

Fig. 2. $Cr_3C_2-20(Ni20Cr)$ Powder X-ray diffraction pattern.

3.2. Microstructural characterization of the coatings

Based on the CBS-SEM images obtained from the cross-section of coatings in 16 samples (Fig. 3), it was determined that, in all

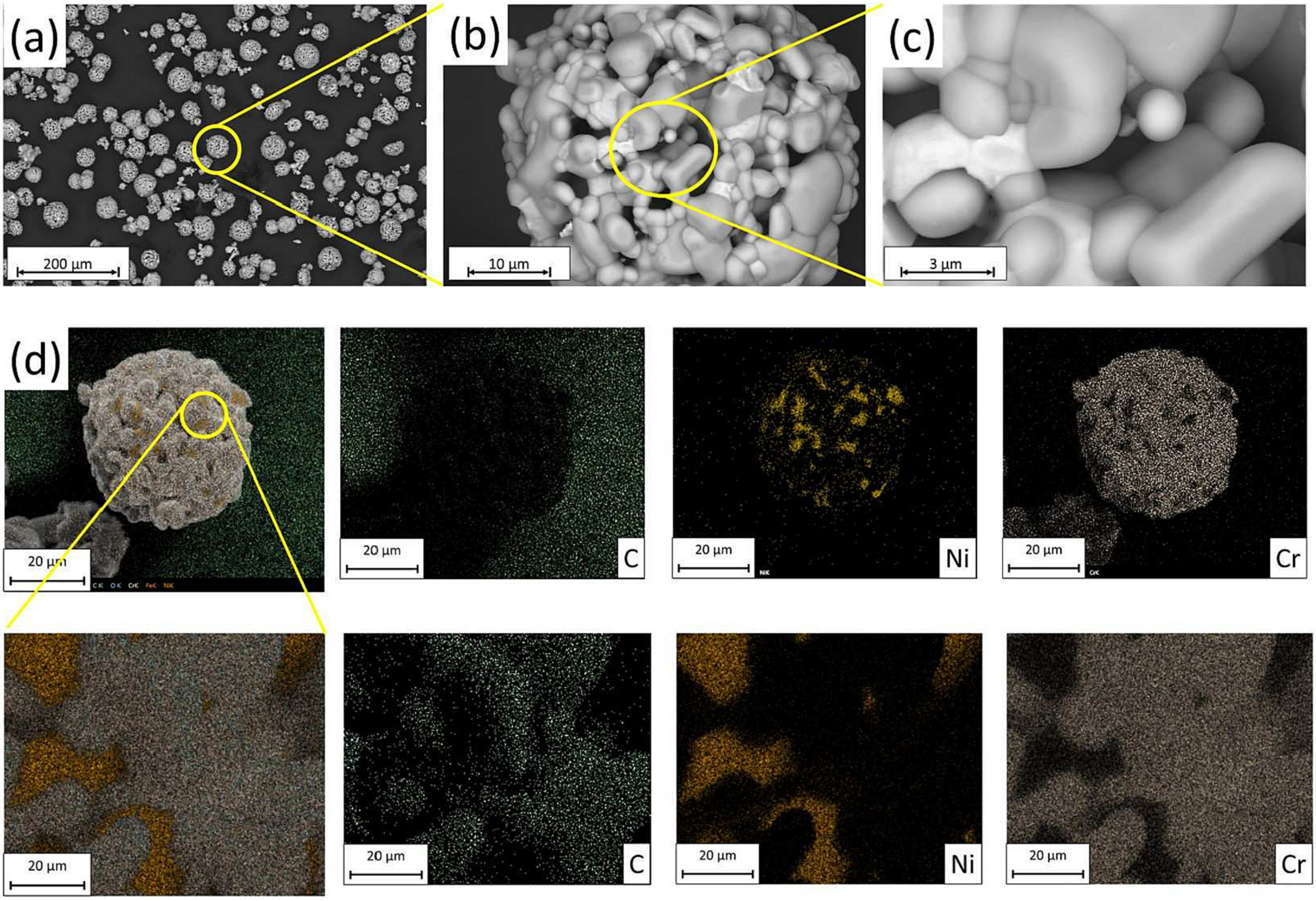

Fig. 1. CBS-SEM images of $Cr_3C_2-20(Ni20Cr)$ powder (a) 500×, (b) 8000×, (c) 30,000× and (d) compositional mapping at 5000×.

Table 2
Summary of the experimental design and results of HVOF coatings.

Application	F/O	Powder flow [*rpm*]	Substrate roughness Ra [μm]	Gun speed [mm/s]	Coating thickness [μm]	Porosity [%]	Surface hardness [*HRC*]	Microhardness [$HV_{0.2}$]
1	0.3	12	18	15	29.48 ± 9.68	31.38 ± 4.08	26.1 ± 2.27	599 ± 35.23
2	0.3	12	28	15	23.20 ± 2.04	8.16 ± 2.20	24.8 ± 1.66	495 ± 23.69
3	0.3	20	28	5	21.54 ± 4.02	27.77 ± 6.61	29.4 ± 1.63	509 ± 21.59
4	0.45	20	18	15	99.28 ± 6.59	1.63 ± 0.49	30.6 ± 3.44	764 ± 34.51
5	0.45	12	28	5	132.76 ± 13.01	1.62 ± 0.33	33.7 ± 2.46	895 ± 27.86
6	0.45	12	28	15	63.40 ± 8.70	2.09 ± 0.49	27.8 ± 4.00	875 ± 17.11
7	0.3	12	18	5	25.95 ± 1.99	24.47 ± 3.43	25.4 ± 0.77	611 ± 61.61
8	0.3	12	28	5	28.89 ± 2.58	21.94 ± 0.90	22.6 ± 2.00	499 ± 13.93
9	0.45	20	28	15	38.80 ± 8.08	2.34 ± 0.37	26.2 ± 5.01	699 ± 59.56
10	0.45	20	28	5	126.92 ± 11.47	4.22 ± 0.61	41.5 ± 1.20	741 ± 50.40
11	0.3	20	18	5	20.01 ± 3.01	27.33 ± 8.57	26.5 ± 3.61	614 ± 14.39
12	0.3	20	28	15	35.35 ± 0.96	32.71 ± 4.37	31.8 ± 1.39	482 ± 28.00
13	0.3	20	18	15	48.12 ± 2.34	19.16 ± 4.20	27.2 ± 3.56	570 ± 63.07
14	0.45	20	18	5	273.77 ± 10.26	1.44 ± 0.12	42.8 ± 0.78	910 ± 34.38
15	0.45	12	18	5	147.80 ± 29.22	1.91 ± 0.20	32.9 ± 3.32	881 ± 23.70
16	0.45	12	18	15	63.18 ± 2.05	3.74 ± 0.33	14.0 ± 1.57	832 ± 83.22

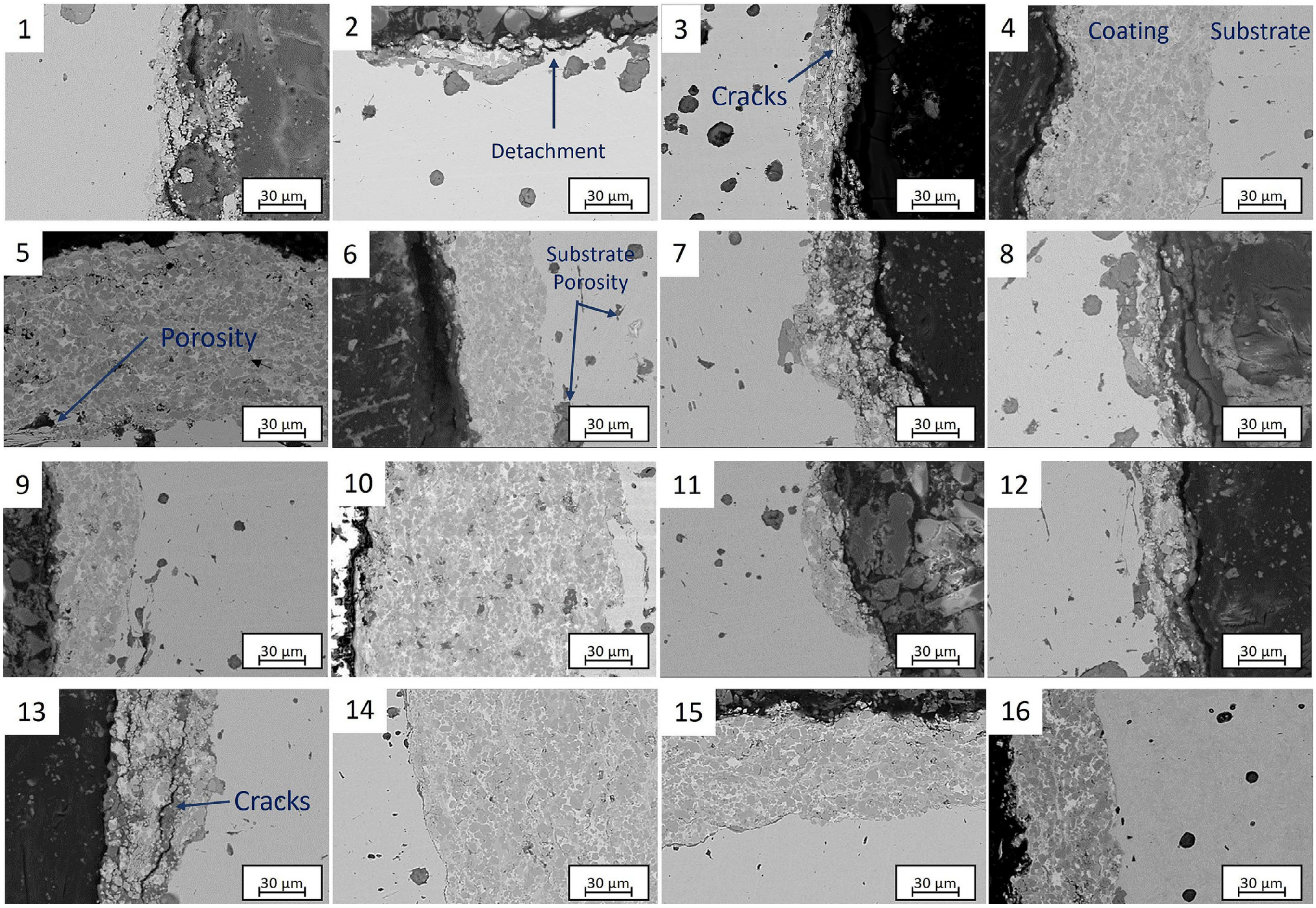

Fig. 3. CBS-SEM images of coating cross-section at 2000×.

cases, there is a homogeneous distribution of phases, where the light gray area is made up of *Ni* and the dark gray section of Cr-carbides.

It should be noted that samples 4, 5, 6, 9, 10, 14, 15, 16, corresponding to a F/O ratio = 0.45, presented a more homogeneous coating as shown in Fig. 3. The other samples with a F/O ratio = 0.3 have poor quality, evidenced by discontinuous and insufficient thickness, as well as particles breaking off from the coating as a sign of lack of cohesion, as seen in samples 1, 2, 7, 8, 11 and 12, as well as the presence of cracks in samples 3 and 13, which, in some cases, caused the layer to detach. Despite this, there is no evidence of cracks in the interface of any of the samples, which shows a good potential adhesion of the powder to the steel. It is observed that the substrate used has a high level of porosity in all specimens.

In some samples, such as sample 10, it can be seen that the coating, despite achieving an adequate level of thickness, has internal porosity greater than 2% due to a lack of cohesion among the particles, which could affect the mechanical performance of the substrate-coating compound. Through SEM images and the summary of results in Table 2, it is clear that the variations in the HVOF operation parameters have different effects on the coatings, making it necessary to statistically investigate the effects related to these parameters. The results obtained from the statistical analysis are discussed in the following subsections.

3.3. Influence of application parameters on thickness

This work was carried out to obtain coatings of 100 μm thickness or more; however, achieving a greater thickness indicates that this is a more efficient process by having a greater number of powder particles deposited on the coating. The ANOVA study performed for the purpose of maximizing thickness is shown in Table 3 for the F/O ratio (A), powder flow (B), surface roughness (C), and gun speed (D) factors. The analysis reveals that the F/O ratio (A) and gun speed (D) are statistically significant factors because they have a $P_{value} < 0.05$. This indicates that the variation in these two factors has a greater influence on thickness, with factor A being the most significant with a lower P_{value}.

This can be better appreciated in the Pareto chart shown in Fig. 4a, where the red line represents the line of significance, showing that the factor with the greatest importance is the F/O ratio, followed by the combination of the AD factors. This interaction indicates that the A and D factors are not independent, as shown in the combined effects graph in Fig. 4b. When the F/O ratio is at its lower level, a greater thickness is achieved with a low gun speed. However, there is no difference in this value, as occurs when changing the F/O to the higher level, where it is seen that a lower gun speed achieves a more positive effect in the coating thickness.

Modifying the F/O ratio helps to generate a combustion process that will deliver greater kinetic energy and raise the temperature of the sprayed powder [59], enabling the particles to reach a semi-melted state. This facilitates the plastic deformation upon impact with the substrate, obtaining greater adhesion and cohesion of the coating. A process that is richer in fuel (F/O = 0.45) allows for a greater thickness.

In the case of speed, a lower speed means that the gun will spend more time in the same area of projection, depositing a larger amount of powder over the coating and, therefore, generating a greater thickness.

Fig. 5 shows the response surfaces obtained from the prediction model with a $R^2_{adjusted} = 82.28\%$, where, based on Eq. (1), the following was obtained:

$$\hat{y} = \begin{aligned} &73.65 + 44.6x_1 + 9.3x_2 - 14.8x_3 - 23.6x_4 - 13x_1x_3 \\ &-28.5x_1x_4 - 12.5x_2x_3 \end{aligned} \tag{3}$$

Fig. 5a exhibits the interaction of the F/O ratio with powder flow, where there is a clear upward trend in thickness with a powder flow of 20 rpm. It also evidence that this factor is completely independent from the F/O ratio, since there is no curvature on the surface, as opposed to surface roughness (Fig. 5b), where there is an interaction between A and C, and it shows a tendency to maximize thickness when there is a low roughness and high F/O ratio.

This same interaction of factors is found between A and D (Fig. 5c) and between B and C (Fig. 5d). In this last case, there is a tendency to maximize thickness when the B factor is at the highest value and C at the lowest, coinciding with the previous graphs. Fig. 5e and f indicate that the gun speed is independent from powder flow and surface roughness, where a lower gun speed tends to maximize thickness.

Table 3
ANOVA results for thickness.

Factors	SS	DF	MS	F	$P_v alue$
A	31806.00	1	31806.00	38.22	0.0003
B	1389.98	1	1389.98	1.67	0.2323
C	3502.57	1	3502.57	4.21	0.0743
D	8875.05	1	8875.05	10.66	0.0114
AC	2692.83	1	2692.83	3.24	0.1097
AD	13016.00	1	13016.00	15.64	0.0042
BC	2510.26	1	2510.26	3.02	0.1206
Error	6657.63	8	832.20		
Total	70450.30	15			

SS: sequential sum of squares, DF: degree of freedom, MS: mean square, F: statistical test.

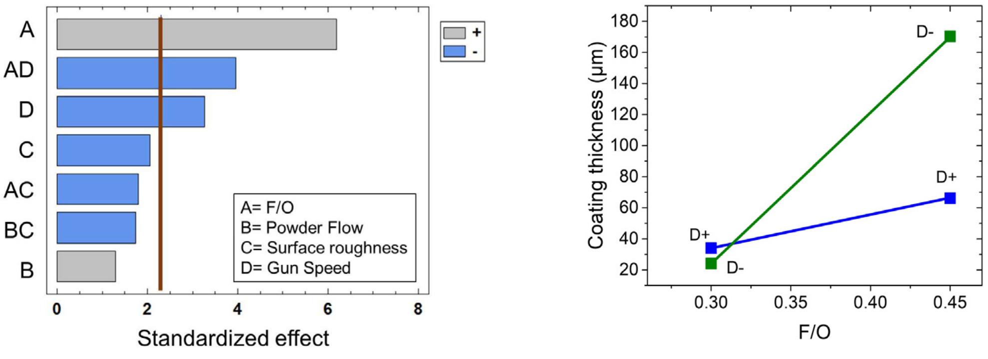

(a)

(b)

Fig. 4. (a) Pareto chart for thickness, and (b) Graph of the interaction between speed and F/O ratio for thickness.

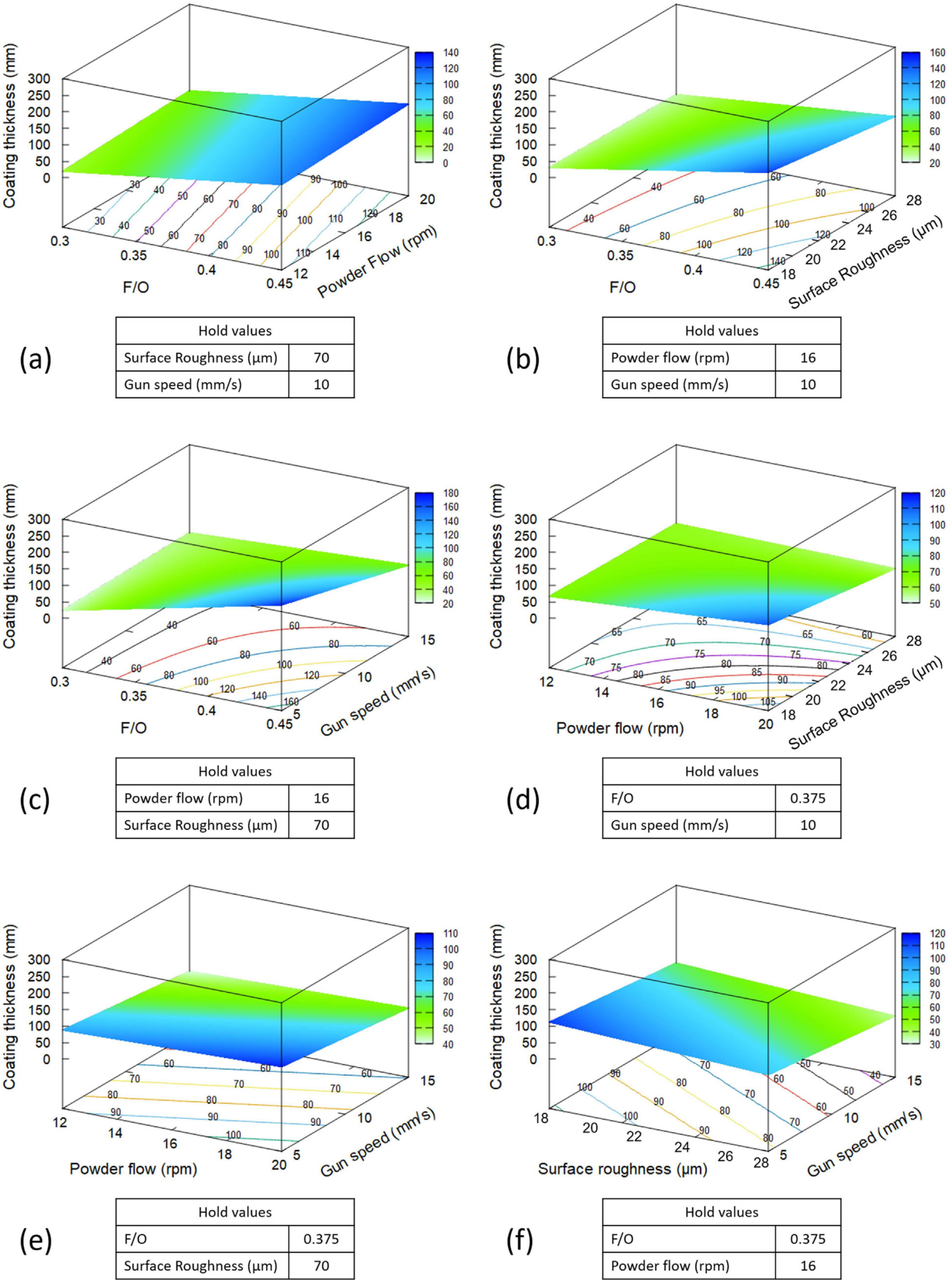

(a)

Hold values	
Surface Roughness (µm)	70
Gun speed (mm/s)	10

(b)

Hold values	
Powder flow (rpm)	16
Gun speed (mm/s)	10

(c)

Hold values	
Powder flow (rpm)	16
Surface Roughness (µm)	70

(d)

Hold values	
F/O	0.375
Gun speed (mm/s)	10

(e)

Hold values	
F/O	0.375
Surface Roughness (µm)	70

(f)

Hold values	
F/O	0.375
Powder flow (rpm)	16

Fig. 5. Thickness response surface based on: (a) F/O and powder Flow, (b) F/O and surface roughness, (c) F/O and gun speed, (d) powder flow and surface roughness, (e) powder flow and gun speed, and (f) surface roughness and gun speed.

Table 4
ANOVA results for porosity.

Factors	SS	DF	MS	F	$P_{v}alue$
A	1890.73	1	1890.73	230.37	0.0000
B	28.33	1	28.33	3.45	0.1055
C	6.52	1	6.52	0.79	0.4025
D	5.63	1	5.63	0.69	0.4349
BC	127.52	1	127.52	15.54	0.0056
ABC	73.57	1	73.57	8.96	0.0201
BCD	68.43	1	68.43	8.34	0.0234
ABCD	74.43	1	74.43	9.07	0.0196
Error	57.45	7	8.21		
Total	2332.61	15			

SS: sequential sum of squares, DF: degree of freedom, MS: mean square, F: statistical test.

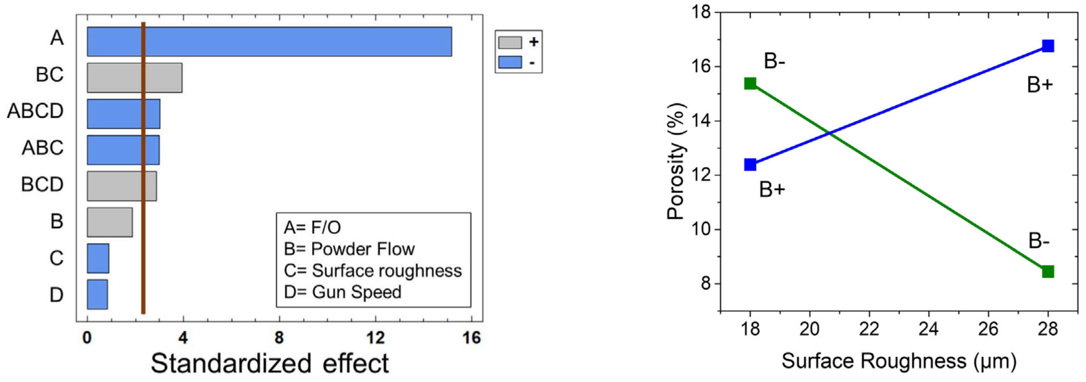

(a) (b)

Fig. 6. (a) Pareto chart for porosity, and (b) Graph of the interaction between surface roughness and powder flow for porosity.

3.4. Influence of application parameters on porosity

The CBS-SEM images of the cross-section in Fig. 3 show a microporosity found in all coatings with the exception of samples 4, 10, 15 and 15. This is possibly caused by the segregation of carbides without an agglomerating matrix Ni to promote the formation of cavities between particles. Moreover, all coatings show a low level of particle cohesion in the area closest to the coating surface, due to the lack of deformation of the last particles projected during the spray process as a result of the absence of a hammering action of other particles that would have a later effect [60].

The result of the ANOVA study (Table 4) exhibits that the F/O ratio is the only independent factor with a significant effect ($P_{value} < 0.05$). It is also the case that some combined effects such as BC, ABC, BCD, and ABCD are statistically significant. As mentioned, the F/O ratio directly influences the energy given to the powder and, therefore, the degree of deformation of the particles, making a denser coating. In this instance, the roughness creates initial conditions for the first sprayed layer to achieve good adhesion, with stable support for the following layers. The quantity of mass deposited in the system depends on the gun speed and powder flow, producing, as a result, along with other variables, a significant effect.

The Pareto chart in Fig. 6a exhibits that the main C and D variables are not significant on their own and that, despite the effect of combined parameters, the F/O ratio is the value with the most significant importance to obtaining a reduction in porosity, since the ratio of 0.45 gives the powder particle greater energy for these to adhere to the coating and get higher thickness values and lower porosity. This indicates that there is better cohesion and adhesion of the coating generated.

The powder flow, despite having a $P_{value} > 0.05$, is more significant in the porosity than in the thickness and appears in all significant combined effects, therefore it is considered for the prediction model obtained according to Eq. (1):

$$\hat{y} = \begin{array}{l} 13.2 - 10.9x_1 + 1.3x_2 + 2.8x_2x_3 - 2.1x_1x_2x_3 + 2.1x_2x_3x_4 \\ -2.2x_1x_2x_3x_4 \end{array} \tag{4}$$

with a $R^2_{adjusted} = 94.72\%$. The BC effect is shown as the combination of parameters with a higher prediction coefficient (2.8). The graph in Fig. 6b shows that, with a high surface roughness value, the lower powder flow generates lower porosity. However, the surface roughness at the lower level results in a denser coating combined with a higher powder flow, which matches the plot in Fig. 5d, and indicates that this combination also produces thicker layers.

Fig. 7a–c show the response surface by analyzing the F/O ratio in combination with other parameters. These results confirm that this factor, at the upper value, produces a reduction in porosity in all cases and has a much greater effect than the others. Fig. 7d evidence the above mentioned combined effect, where there is a green area on the response surface that is larger for powder flow (negative) and substrate roughness (positive), but also, a green area for powder flow (positive) with a surface roughness at its lower value. Then, Fig. 7e and f show nearly no slope on the surfaces, indicating that these parameters in combination have no relevant effect on porosity.

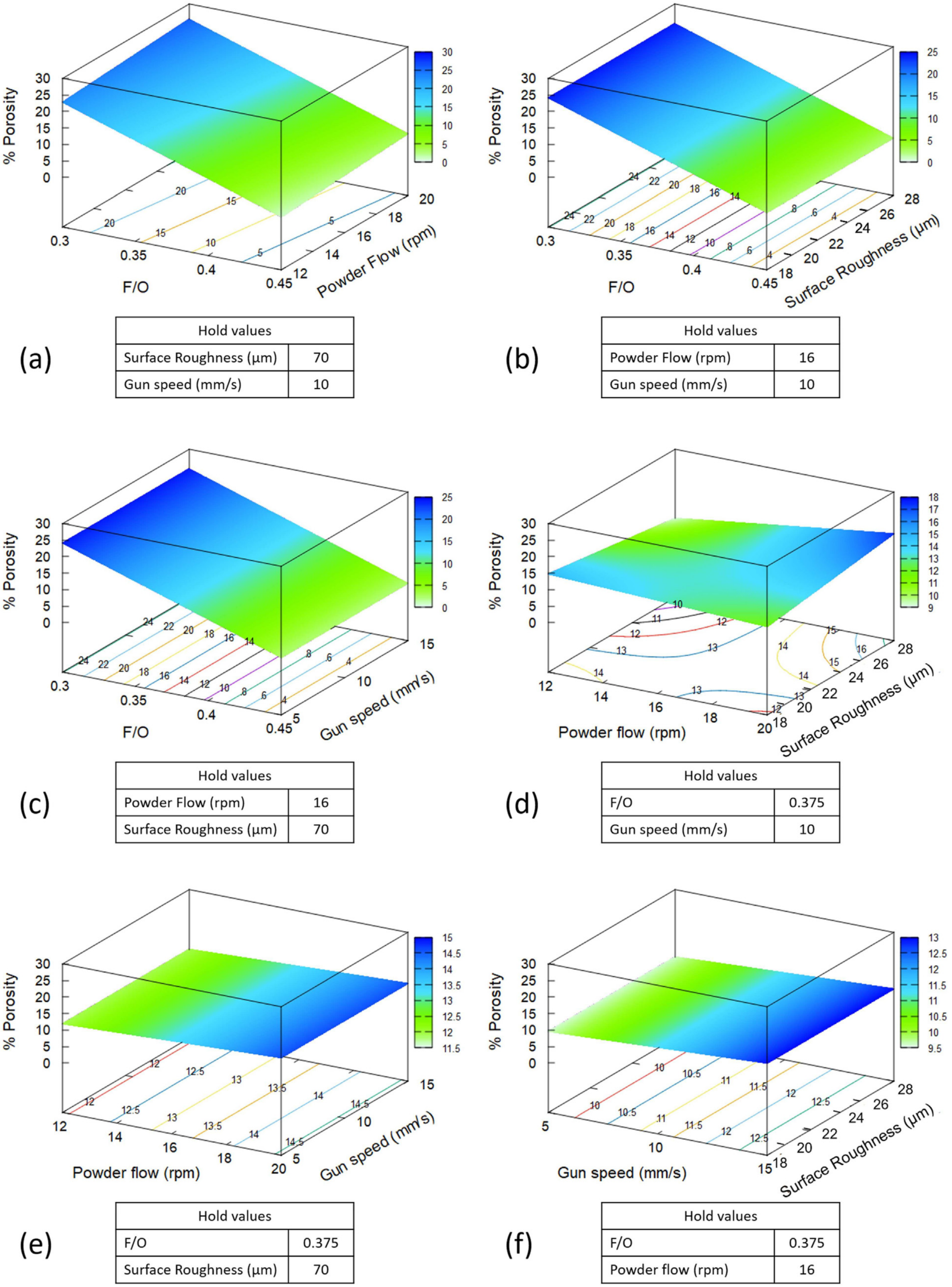

(a)

Hold values	
Surface Roughness (μm)	70
Gun speed (mm/s)	10

(b)

Hold values	
Powder Flow (rpm)	16
Gun speed (mm/s)	10

(c)

Hold values	
Powder Flow (rpm)	16
Surface Roughness (μm)	70

(d)

Hold values	
F/O	0.375
Gun speed (mm/s)	10

(e)

Hold values	
F/O	0.375
Surface Roughness (μm)	70

(f)

Hold values	
F/O	0.375
Powder flow (rpm)	16

Fig. 7. Porosity response surface based on: (a) F/O and powder Flow, (b) F/O and surface roughness, (c) F/O and gun speed, (d) powder flow and surface roughness, (e) powder flow and gun speed, and (f) surface roughness and gun speed.

Table 5
ANOVA results for surface hardness.

Factors	SS	DF	MS	F	$P_v alue$
A	79.55	1	79.55	10.01	0.0101
B	149.35	1	149.35	18.79	0.0015
D	134.12	1	134.12	16.87	0.0021
AD	212.55	1	212.55	26.74	0.0004
ABC	63.98	1	63.98	8.05	0.0176
Error	79.48	10	7.95		
Total	719.03	15			

SS: sequential sum of squares, DF: degree of freedom, MS: mean square, F: statistical test.

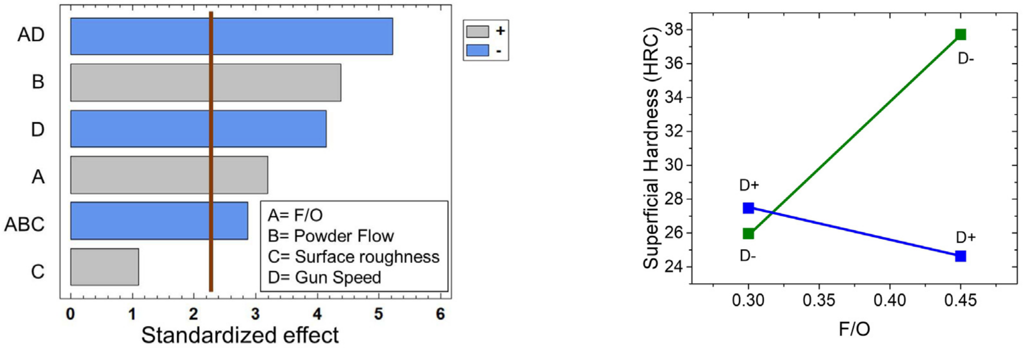

(a) (b)

Fig. 8. (a) Pareto chart for surface hardness, and (b) Graph of the interaction between speed and F/O ratio for surface thickness.

3.5. Influence of application parameters on surface hardness

The results of the ANOVA study (Table 5) show that the main factors are A, B, and D, while the combined factors AD and ABC are significant ($P_{value} < 0.05$). The Pareto chart in Fig. 8a exhibits the most significant factor as AD interaction. This interaction between F/O and gun speed is also a significant factor for thickness. However, unlike thickness and porosity, the independent F/O ratio parameter is not the most influential parameter. In fact, powder flow and gun speed have a lower P_{value}, which means that they have a greater effect on this variable studied.

The C factor is discarded for the prediction model since this has little significance and was added as degree of error, resulting in the following model according to Eq. (1):

$$\hat{y} = 29 + 2.2x_1 + 3.1x_2 - 2.9x_4 - 3.6x_1x_4 - 2x_1x_2x_3 \tag{5}$$

where only the parameters shown in Table 5 are used with $R^2_{adjusted} = 83.42\%$. This equation shows that all coefficients are close values, indicating their high level of dependence.

Fig. 8b exhibits the interaction graph for the AD factor where, with a F/O ratio of 0.3, the effect of gun speed is lower. However, when the F/O ratio is raised to 0.45, the change in speed generates a significant effect on surface hardness, achieving a higher value with a speed of 5 mm/s. This is because a low speed and a high F/O ratio generate greater coating thickness, which gives the substrate-coating compound a better structural resistance since it has a greater proportion of hard material.

In the graph on the response surface of hardness as a function of the A and B parameters (Fig. 9a), the absence of curvature can be seen, which indicates that these two factors are independent. Likewise, as the F/O ratio increases, the powder flow also increases the hardness value. Fig. 9b shows a surface curvature where there is a change from the green area to the blue area, indicating greater hardness when the F/O ratio rises and the gun speed drops.

Finally, Fig. 9c exhibits a surface without curvature between the powder flow and gun speed, indicating independence in the factors. Once again, an increase in the coating properties is seen when the powder flow increases and the gun speed decreases.

3.6. Influence of application parameters on microhardness

The optical microscopy images in Fig. 10 show the profile of indentations made from the coating surface to the substrate and carried out on the interface. When using a load of 200 gf over the coatings with a F/O ratio = 0.45, a larger size imprint is made than those produced with 50 gf, as shown in Figs. 10b and 13c. The highest load allows for values that are closer to the actual value of the coating, with less variation among the indentations. To these coatings with greater thickness and density, loads of up to 1000 gf are applied on the interface without cracking, indicating excellent adhesion.

For the case of less thick coatings, corresponding to the F/O ratio = 0.3, the load of 50 gf generates measurements for comparing them and obtaining the effects of the variables on these coatings.

It should be noted that the AISI 4140 steel substrate, unlike the coating, is a more ductile material, and has a larger area indentation than the coating and zones where the material moves, as shown in Fig. 10a, due to the profile of the forces to which it is subject thanks to the insertion of the indenter. This may be understood through the difference in hardness that, in the case of the substrate, is 270 ± 10.60 HV on average, while for the coating is up to 910 ± 34.38 HV. In the case of the interface, microhardness represents 63 ± 7.07% of the microhardness of the coating.

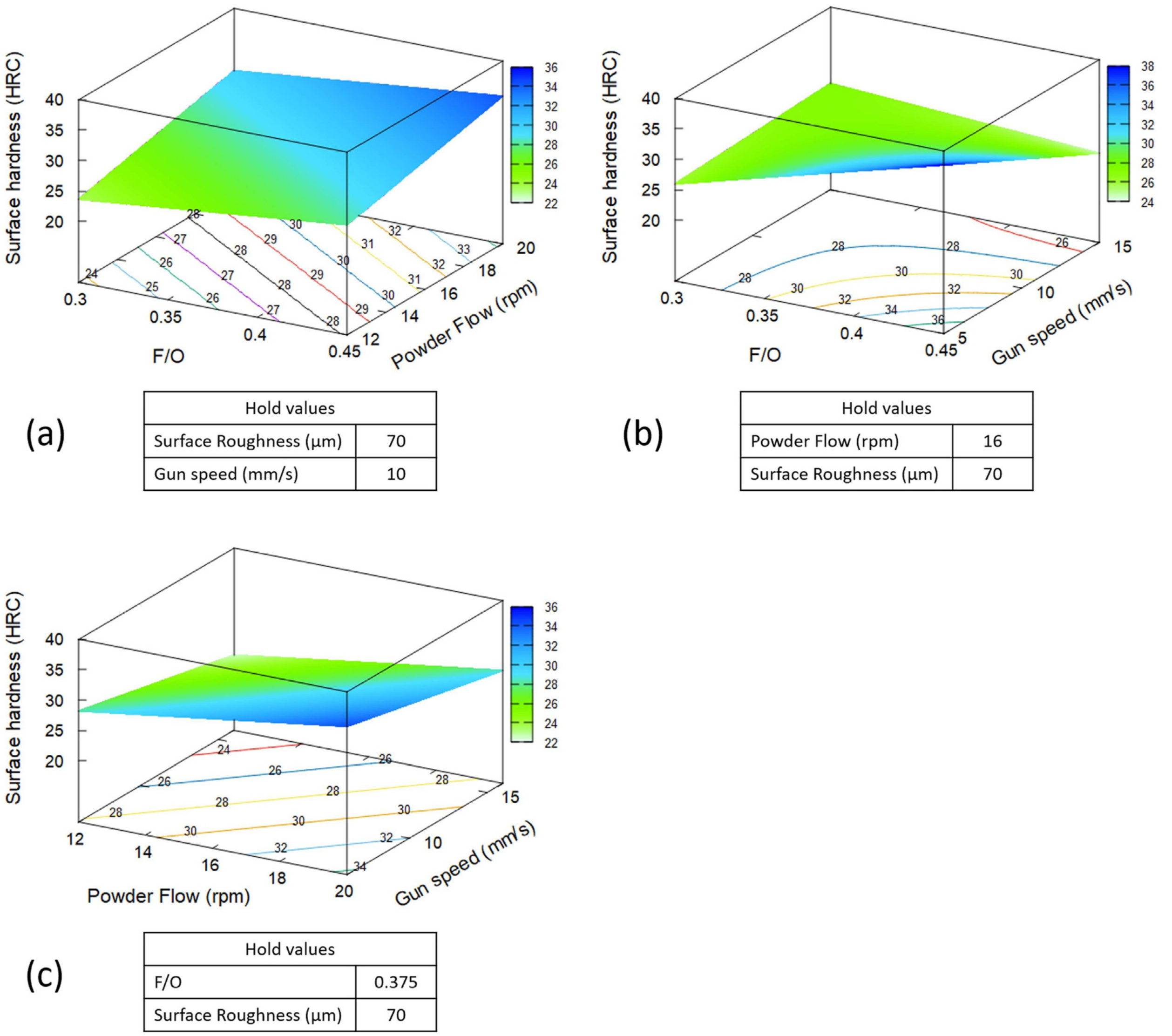

(a)

Hold values	
Surface Roughness (μm)	70
Gun speed (mm/s)	10

(b)

Hold values	
Powder Flow (rpm)	16
Surface Roughness (μm)	70

(c)

Hold values	
F/O	0.375
Surface Roughness (μm)	70

Fig. 9. Surface hardness response surface based on: (a) powder flow and surface roughness, (b) powder flow and gun speed, and (c) surface roughness and gun speed.

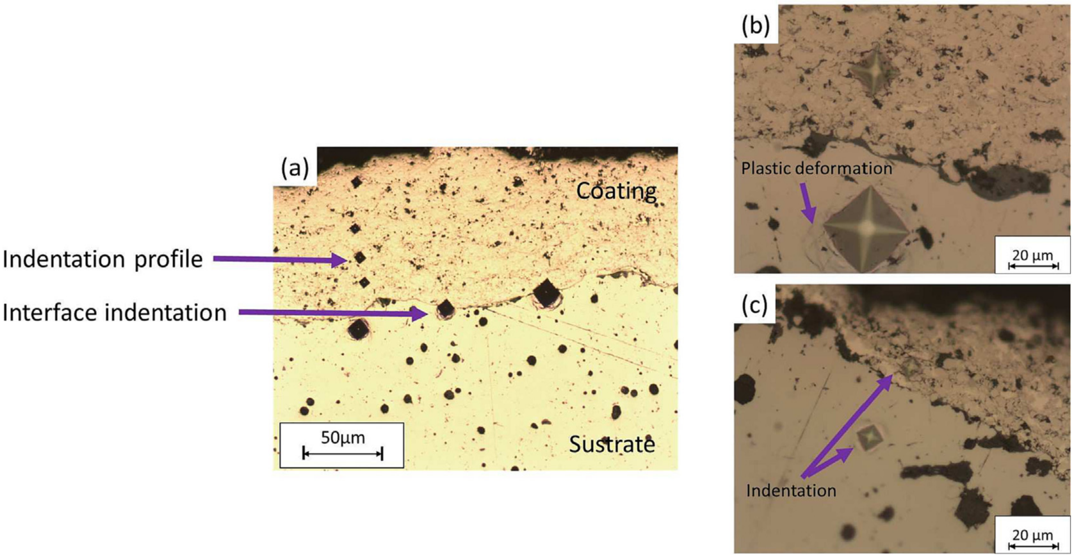

Fig. 10. (a) Optical microscopy of microhardness profile in sample 14, (b) Microindentations profile of sample 14 with HV0.2 scale, and (c) Microindentations profile of sample 3 with HV0.05 scale.

Table 6
ANOVA results for microhardness.

Factors	SS	DF	MS	F	P_value
B	9900.25	1	9900.25	5.41	0.0451
C	21462.30	1	21462.30	11.72	0.0076
D	7396.00	1	7396.00	4.04	0.0754
AB	7225.00	1	7225.00	3.94	0.0783
BC	4489.00	1	4489.00	2.45	0.1519
Blocks + A	307470.00	1	307470.00	167.88	0.0000
Error	16483.30	9	1831.47		
Total	374425.85	15			

SS: sequential sum of squares, DF: degree of freedom, MS: mean square, F: statistical test.

To perform the statistical study of the results obtained, two blocks generated by the A factor were used, because the F/O ratios is the factor that most greatly influences thickness and, therefore, the load of indentation applied. This will allow for the comparison of all coatings and calculation of the effect of the variables combined with this factor, despite being measured with different loads and not being able to calculate the pure effect of factor A.

Table 6 exhibits the results of the ANOVA study, where the B and C factors are significant ($P_{value} < 0.05$) just like the blocks factor.

The Pareto chart in Fig. 11 confirms that the surface roughness is more significant, followed by powder flow. Moreover, AB and BC are the combined effects with greater significance, with a $P_{value} > 0.05$, and are considered in the prediction model. It should be noted that all factors are negative, which indicates that both B and C at their lower level help maximize the microhardness of the coating. In the case of roughness, while there are some authors that mention that an increase in roughness leads to greater adhesion [25], this is only applicable to roughnesses of $Ra < 7$ µm, since at higher roughnesses, this parameter is no longer significant for adhesion [61]. In this study, the higher surface roughness value ($R_a = 28$ µm) makes the opposite effect; the coatings tend to generate a lower coating adhesion, demonstrated by greater thicknesses and low porosity, which causes microhardness to drop.

The large-activated area of the colliding powder particles and the roughness of the substrate surface tends to promote mechanical interlocking [62]. Large surface roughness value does not promote adhesion due to non-uniform stress and temperature distributions at the interface between the particle and the substrate [63].

Splat formation is enhanced when the powder flow is controlled. If the flow is too low, the particles can heat up excessively and cause metal reduction process that result in carbide agglomeration and crack formation. Furthermore, if too much powder is added, the particles will not be able to enter a semi-fused state, preventing them to deform and adhere to the coating [64].

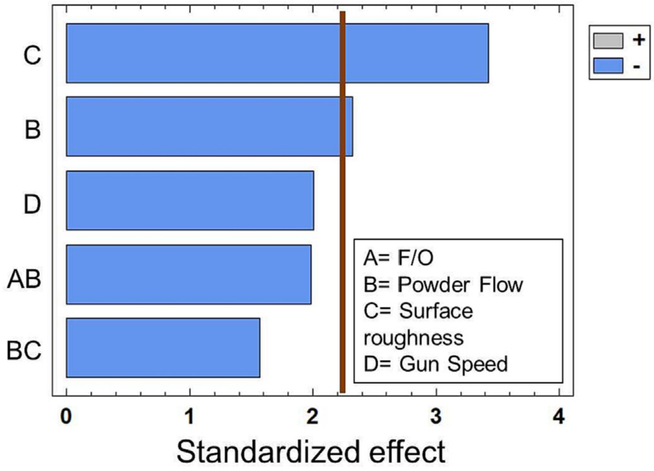

Fig. 11. Pareto chart for microhardness.

Therefore, powder flow and surface roughness are intimately related to coating interfaces and cohesion. Having particles adhere better to the substrate and each other results in higher densification and microhardness coatings.

It is known that the value of microhardness increases due to the high density, low porosity, and high resistance to cohesion [27], and that the parameter with the greatest significant effect on these properties in comparison to the other parameters is the F/O ratio, which yields better results at its lower value. It is inferred that, despite the fact that this factor is confused with blocks, it generates the main effect due to this combined effect (blocks + A), so it is considered that the F/O ratio is also significant and, therefore, is added to the prediction model, to obtain according to Eq. (1):

$$\hat{y} = 696.8 + 138.6x_1 - 24.9x_2 - 36.6x_3 - 10x_4 - 21.3x_1x_2 - 16.75x_2x_3 \tag{6}$$

with a $R^2_{adjusted} = 92.7\%$ where, the coefficient of the factor x_1 which represents the F/O ratio, is positive, showing that microhardness, represented by $\hat{y}$, will increase when this parameter is at its upper limit.

Fig. 12a shows the response surface of microhardness as a function of powder flow and surface roughness, where a slight curvature is observed, marking a green zone of reduced microhardness when these two parameters are combined at their upper level, and the same is increasing when they are at their lower level. Fig. 12b exhibits a surface without curvature, indicating that the gun speed and powder flow are entirely independent and with the maximization of microhardness when both are at their lower value. This response surface behavior is similar to surface roughness and gun velocity observed in Fig. 12c microhardness maximization when both are at their lower value.

3.7. Selection of parameters

For the selection of optimal parameters according to this study, the effect of these on each of the properties measured has been analyzed.

In the case of the F/O ratio, there is a large influence on thickness, achieving coatings greater than 100 µm in all cases where F/O = 0.45. For this same factor level, porosity is reduced by up to 95.6%. Using the uncoated substrate hardness (20 HRC) as a reference, the coatings with a greater increase in hardness are 7 and 14, doubling the value to 41 and 43 HRC respectively. Both samples coincide with a F/O ratio at the higher level.

For powder flow, in the case of thickness and porosity, it is not significant in either of the two properties, although, when studying the response surfaces, this factor generally tends to maximize thickness and minimize porosity where the powder feeder is deliv-

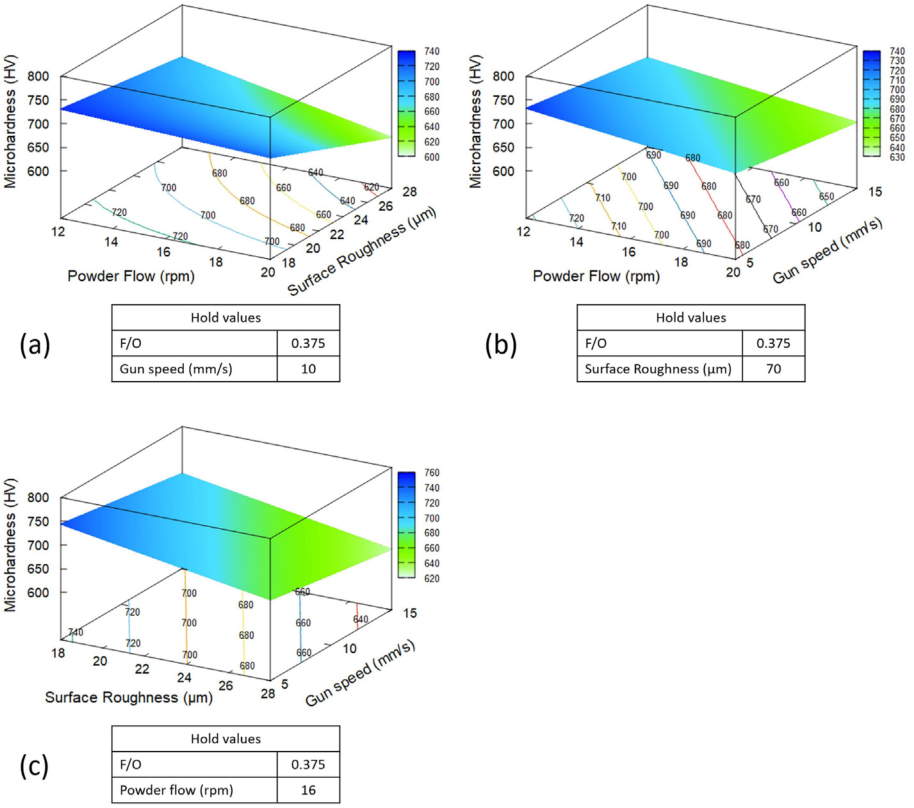

(a)

Hold values	
F/O	0.375
Gun speed (mm/s)	10

(b)

Hold values	
F/O	0.375
Surface Roughness (µm)	70

(c)

Hold values	
F/O	0.375
Powder flow (rpm)	16

Fig. 12. Microhardness response surface based on: (a) F/O and powder flow, (b) F/O and gun speed, and (c) powder flow and gun speed.

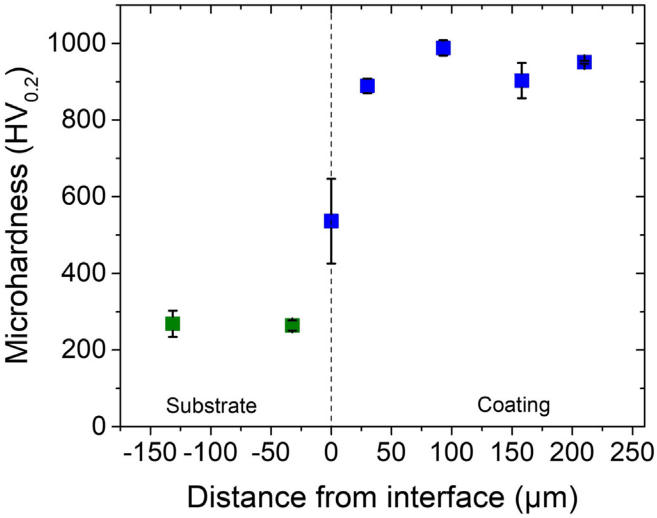

Fig. 13. Microhardness profile of sample 14.

ering a greater amount of powder (20*rpm*). This parameter also tends to produce a greater thickness, making it significant in this property and producing an increase of up to 114% over the substrate.

In the case of microhardness, powder flow is also significant, with a tendency to maximize the value when the feeder spins at 12 rpm, although the main effect on this property is substrate roughness, delivering a greater microhardness with a $R_a = 18$ µm, whose value tends to produce greater thicknesses.

Table 7
Parameters and summary of sample 14 properties.

Parameter	Value
F/O Ratio	0.45
Powder flow [rpm]	20
Roughness Ra [μm]	18
Gun speed [mm/s]	5
Properties	
Thickness [μm]	273.77 ± 10.26
Porosity [%]	1.44 ± 0.12
Surface hardness [HRC]	42.8 ± 0.78
Microhardness	910 ± 34.38

When analyzing gun speed, a speed of 5 mm/s makes significantly greater thicknesses. Moreover, this parameter interacts positively with the F/O ratio = 0.45, which also affects porosity. This effect is also repeated for surface hardness, where an increase in speed causes a decrease of 14% on average in surface hardness.

For these reasons, the parameters in Table 7 are selected, and which also shows the properties of sample 14 which correspond to optimal factors. Fig. 13 exhibits the hardness profile found in this sample throughout its cross-section. The SEM images for this sample confirm a high densification of the coating (average porosity of 1.44%), with greater thickness ($\sim$ 274 µm), and homogeneous properties in its cross-section, with no discontinuities.

An inspection of the diffractogram of the coating deposited on sample 14, shown in Fig. 14, reveals that the compounds identified in the powder diffractogram (Fig. 3) are maintained. It is shown that there is an amorphization of the structures evidenced by wider peaks; this may be because there is a high plastic deformation of the projected powder particles. Additionally, peaks are

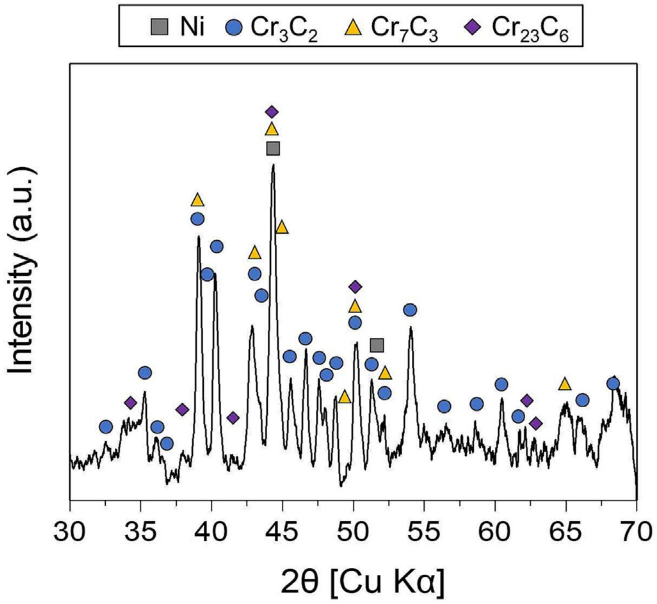

Fig. 14. $Cr_3C_2 - 20(Ni20Cr)$ sample 14 diffraction pattern.

detected at angles 33.6°, 37.7°, 62.1°, and 62.8°, corresponding to a higher presence of $Cr_{23}C_6$. This is caused by the elevated temperatures subjected to the filler material during the process. However, no evidence of substantial changes in the power structure that could modify the macroscopic properties of the coating is found.

Experimental 2^4 has been determined to be an adequate design for improving hard coatings deposited by HVOF at an industrial level. The effect of operation parameters, such as F/O ratio, powder flow, substrate roughness, and gun speed, is related to the relevant properties for final application, such as thickness, porosity, surface hardness, and microhardness. The best conditions can be achieved by performing an optimization process after designing experiments that allow knowing the behavior of the parameters.

4. Conclusions

This study establishes the foundation for generating $Cr_3C_2 - 20(Ni20Cr)$ coatings on a AISI 4140 substrate using the HVOF technique.

According to this study, the oxygen-fuel ratio (F/O) is the most influential variable for the formation of quality coatings. An increase from 0.3 to 0.45 in this variable produces an increase in 90 μm average thickness, $5HRC$ surface hardness and $60HV$ microhardness, as well as a reduction in internal porosity of up to 22%.

On the other hand, decreasing gun speed from 15 to $5mm/min$, tends to raise dwell time, which results in more amount of particles being deposited under the test conditions, resulting in 50 μm average thickness increase, and 22% surface hardness improvement, without necessarily reducing porosity.

Roughness and powder flow have a greater effect on both surface hardness and microhardness in the cross-section. The surface roughness controls the degree of adhesion of the first layer of powder to the substrate. Despite the fact that literature evidence a trend towards an increase in this property with greater roughness, this study showed a higher value in this parameter actually caused the opposite effect when working with high values of Ra.

A higher powder flow produces greater surface hardness and, combined with a F/O ratio of 0.45, reduces the porosity percentage found by up to 30%, taking the worst condition as a reference.

Considering the results of the samples analyzed, the following yielded better characteristics for generating homogeneous and good-quality coatings are: F/O ratio of 0.45, powder flow from the feeder at 20 rpm, gun speed of 5 mm/s, and roughness $R_a = 18\ \mu m$. With these values, coatings were obtained with thicknesses $> 200\ \mu m$, porosities $< 1.5\%$, surface hardness increases over 100% compared to the uncoated substrate, and microhardness in the cross-section of over 900 HV.

Funding sources

This work was supported by the Dirección de Investigación, Innovación y Emprendimiento of Universidad Técnica Federico Santa María [Grant No. PI_LI_19_10], and the funding provided by the Agencia Nacional de Investigación y Desarrollo (ANID) of the Chilean government [Grant No. FONDECYT 1180702, FONDEQUIP EQM150101, Anillo (ACT192023).

CRediT authorship contribution statement

S. Sauceda: Formal analysis, Writing – review & editing. **S. Lascano:** Resources, Writing – review & editing, Visualization, Supervision. **J. Núñez:** Project administration, Methodology, Writing – review & editing, Funding acquisition. **C. Parra:** Resources, Writing – review & editing. **C. Arévalo:** Resources, Formal analysis, Writing – review & editing, Visualization. **L. Béjar:** Resources, Visualization, Writing – review & editing.

Declaration of Competing Interest

The authors declare that they have no known competing financial interests or personal relationships that could have appeared to influence the work reported in this paper.

Acknowledgment

The authors would like to thank and dedicate this article to our beloved friend and colleague who carried out this work with us – Luis Bejar, who unfortunately passed away after finishing this work. The authors thank the laboratory technicians Jesus Pinto at Universidad de Sevilla (Spain), Claudio Aravena, and Gabriel Cornejo at Universidad Técnica Federico Santa María (Chile) for their support in carrying out the microstructural characterization and mechanical testing. The authors would like to thank the editors and anonymous reviewers for providing insightful suggestions and comments to improve the quality of research paper.

References

[1] J. Cao, X. Chen, X. Zhang, Y. Gao, X. Zhang, S. Kumar, Overview of remanufacturing industry in China: Government policies, enterprise, and public awareness, J. Clean. Prod. 242 (2020) (2020), https://doi.org/10.1016/j.jclepro.2019.118450. URL: https://linkinghub.elsevier.com/retrieve/pii/S0959652619333207 118450.

[2] J.R. Davis et al., Handbook of thermal spray technology, ASM Int. 2004 (2004).

[3] J.Y. Du, Y.L. Li, F.Y. Li, X.J. Ran, X.Y. Zhang, X.X. Qi, Research on the high temperature oxidation mechanism of Cr3C2-NiCrCoMo coating for surface remanufacturing, J. Mater. Res. Technol. 10 (2021) (2021) 565–579, https://doi.org/10.1016/j.jmrt.2020.12.049. URL: https://linkinghub.elsevier.com/retrieve/pii/S2238785420321256.

[4] E. DIN, 657: Thermal spraying–terminology, Classification. Norm 6 (2005).

[5] M. Oksa, E. Turunen, T. Suhonen, T. Varis, S.-P. Hannula, Optimization and Characterization of High Velocity Oxy-fuel Sprayed Coatings: Techniques, Materials, and Applications, Coatings 1 (1) (2011) 17–52 (2011). doi:10.3390/coatings1010017. URL: http://www.mdpi.com/2079-6412/1/1/17.

[6] J.A. Picas, M. Punset, S. Menargues, M. Campillo, M. Teresa Baile, A. Forn, The influence of heat treatment on tribological and mechanical properties of HVOF sprayed CrC-NiCr coatings, International Journal of Material Forming 2 (SUPPL. 1) (2009) 225–228 (2009). doi:10.1007/s12289-009-0466-0.

[7] V. Matikainen, H. Koivuluoto, P. Vuoristo, A study of Cr3C2-based HVOF- and HVAF-sprayed coatings: Abrasion, dry particle erosion and cavitation erosion resistance, Wear 446–447 (2020) (2020), https://doi.org/10.1016/j.wear.2020.203188. URL: https://linkinghub.elsevier.com/retrieve/pii/S0043164819315947 203188.

[8] J. Berget, T. Rogne, E. Bardal, Erosion-corrosion properties of different WC-Co-Cr coatings deposited by the HVOF process-influence of metallic matrix composition and spray powder size distribution, Surf. Coat. Technol. 201(18) (2007) 7619–7625 (2007). doi:10.1016/j.surfcoat.2007.02.032. URL: https://linkinghub.elsevier.com/retrieve/pii/S0257897207001417.

[9] G. Bolelli, A. Colella, L. Lusvarghi, P. Puddu, R. Rigon, P. Sassatelli, V. Testa, Properties of HVOF-sprayed TiC-FeCrAl coatings, Wear 2019 (2019) 36–51, https://doi.org/10.1016/j.wear.2018.11.002.

[10] R. Pileggi, M. Tului, D. Stocchi, S. Lionetti, Tribo-corrosion behaviour of chromium carbide based coatings deposited by HVOF, Surf. Coat. Technol. 268 (2015) (2015) 247–251, https://doi.org/10.1016/j.surfcoat.2014.10.007.

[11] S.G. Sapate, N. Tangselwar, S.N. Paul, R.C. Rathod, S. Mehar, D.S. Gowtam, M. Roy, Effect of Coating Thickness on the Slurry Erosion Resistance of HVOF-Sprayed WC-10Co-4Cr Coatings, J. Therm. Spray Technol. 2021 (2021) 1–15, https://doi.org/10.1007/s11666-021-01190-2.

[12] J. Ren, R. Ahmad, G. Zhang, Y. Rong, Y. Ma, A parametric simulation model for HVOF coating thickness control, Int. J. Adv. Manuf. Technol. 116(1–2) (2021) 293–314 (2021). doi:10.1007/s00170-021-07429-0.

[13] S. Thermsuk, P. Surin, Optimization parameters of WC-12Co HVOF sprayed coatings on SUS 400 stainless steel, in: Procedia Manufacturing, vol. 30, Elsevier B.V., 2019, pp. 506–513 (2019). doi:10.1016/j.promfg.2019.02.071. URL: https://linkinghub.elsevier.com/retrieve/pii/S2351978919301027.

[14] J. Mehta, V.K. Mittal, P. Gupta, Role of thermal spray coatings on wear, erosion and corrosion behavior: A review, J. Appl. Sci. Eng. 20(4) (2017) 445–452 (2017). doi:10.6180/jase.2017.20.4.05. URL: http://jase.tku.edu.tw/articles/jase-201712-20-4-05.

[15] P. Nguyen Vinh, N. Dang Thien, C. Le Chi, Evaluating the effect of hvof sprayed wc-10co-4cr and hard chromium electroplated coatings on fatigue strength of axle-shaped machine parts, in: International Conference on Engineering Research and Applications, Springer, 2018, pp. 309–317 (2018). doi:10.1007/978-3-030-04792-4_41.

[16] M. Gui, R. Eybel, S. Radhakrishnan, F. Monerie-Moulin, R. Raininger, P. Taylor, Residual Stress in HVOF Thermally Sprayed WC-10Co-4Cr Coating in Landing Gear Application, J. Therm. Spray Technol. 28(6) (2019) 1295–1307 (2019). doi:10.1007/s11666-019-00894-w.

[17] A. Scrivani, S. Ianelli, A. Rossi, R. Groppetti, F. Casadei, G. Rizzi, A contribution to the surface analysis and characterisation of HVOF coatings for petrochemical application, Wear 250 (1–12) (2001) 107–113 (oct 2001). doi:10.1016/S0043-1648(01)00621-4. URL: https://linkinghub.elsevier.com/retrieve/pii/S0043164801006214.

[18] S. Hong, Y. Wu, J. Wu, Y. Zhang, Y. Zheng, J. Li, J. Lin, Microstructure and cavitation erosion behavior of HVOF sprayed ceramic-metal composite coatings for application in hydro-turbines, Renew. Energy 164 (2021) 1089–1099 (feb 2021). doi:10.1016/j.renene.2020.08.099. URL: https://linkinghub.elsevier.com/retrieve/pii/S0960148120313422.

[19] E. Carneiro, J.D. Castro, S.M. Marques, A. Cavaleiro, S. Carvalho, REACH regulation challenge: Development of alternative coatings to hexavalent chromium for minting applications, Surf. Coat. Technol. 418 127271 (jul). doi:10.1016/j.surfcoat.2021.127271. URL: https://linkinghub.elsevier.com/retrieve/pii/S0257897221004.

[20] Y. Wang, D. Zhou, H. Huang, Y. Chang, Effects of the surface texture in a compressor impeller shaft on its remanufacturing using HVOF, Int. J. Adv. Manuf. Technol. 93 (5–8) (2017) 2423–2432 (nov 2017). doi:10.1007/s00170-017-0644-z.

[21] H. Lu, Y. Li, F. Li, X. Zhang, C. Zhang, J. Du, Z. Li, X. Ran, J. Li, W. Wang, Damage mechanism and evaluation model of compressor impeller remanufacturing blanks: A review, Front. Mech. Eng. 14(4) (2019) 402–411 (2019). doi:10.1007/s11465-019-0548-8.

[22] S. Tailor, N. Vashishtha, A. Modi, S.C. Modi, Structural and mechanical properties of HVOF sprayed Cr3C2-25% NiCr coating and subsequent erosion wear resistance, Mater. Res. Express 6(7) (2019) 76435 (2019). doi:10.1088/2053-1591/ab1947.

[23] X. Ding, Y. Huang, C. Yuan, Z. Ding, Deposition and cavitation erosion behavior of multimodal WC-10Co4Cr coatings sprayed by HVOF, Surf. Coat. Technol. 392 (2020) 125757 (jun 2020). doi:10.1016/j.surfcoat.2020.125757. URL: https://linkinghub.elsevier.com/retrieve/pii/S025789722.

[24] S.P. Dora, S. Chintada, T.R. Palukuri, S.R. Pujari, Energy dissipation in WC-Co coated A356.2/RHA composites, Eng. Sci. Technol. 23(5) (2020) 1285–1290 (oct 2020). doi:10.1016/J.JESTCH.2020.04.001. URL: https://linkinghub.elsevier.com/retrieve/pii/S2215098620300409.

[25] Y.Y. Wang, C.J. Li, A. Ohmori, Influence of substrate roughness on the bonding mechanisms of high velocity oxy-fuel sprayed coatings, Thin Solid Films 485 (1–2) (2005) 141–147 (2005). doi:10.1016/j.tsf.2005.03.024. URL: https://linkinghub.elsevier.com/retrieve/pii/S0040609005002841.

[26] L. Tang, J. jie Kang, P. fei He, S. yu Ding, S. ying Chen, M. Liu, Y. cheng Xiong, G. zheng Ma, H. dou Wang, Effects of spraying conditions on the microstructure and properties of NiCrBSi coatings prepared by internal rotating plasma spraying, Surf. Coat. Technol. 374 (2019) 625–633 (sep 2019). doi:10.1016/j.surfcoat.2019.06.056. URL: https://linkinghub.elsevier.com/retrieve/pii/S0257897219306796.

[27] N.C. Reddy, B.S. Kumar, H.N. Reddappa, M.R. Ramesh, P.G. Koppad, S. Kord, HVOF sprayed Ni3Ti and Ni3Ti+(Cr3C2+20NiCr) coatings: Microstructure, microhardness and oxidation behaviour, J. Alloys Compd. 736 236–245 (mar). doi:10.1016/j.jallcom.2017.11.131. URL: https://linkinghub.elsevier.com/retrieve/pii/S0925838817338896.

[28] E. Vural, The Study of Microstructure and Mechanical Properties of Diesel Engine Piston Coated with Carbide Composites by Using HVOF Method (oct 2020). doi:10.1007/s12666-020-02055-y.

[29] C.H. Yeh, N. Jeyaprakash, C.H. Yang, Temperature dependent elastic modulus of HVOF sprayed Ni-5 nondestructive laser ultrasound technique, Surf. Coat. Technol. 385 (January) (2020) 125404 (2020). doi:10.1016/j.surfcoat.2020.125404.

[30] S.Y. Zhachkin, A.I. Zavrazhnov, N.A. Penkov, G.V. Kudryavtsev, P.V. Tsisarenko, About Determing the Microhardness of Composite Coatings, Mater. Sci. Forum 1037 (2021) (2021) 486–493, https://doi.org/10.4028/WWW.SCIENTIFIC.NET/MSF.1037.486.

[31] A. Valarezo, W.B. Choi, W. Chi, A. Gouldstone, S. Sampath, Process control and characterization of NiCr coatings by HVOF-DJ2700 system: A process map approach, J. Therm. Spray Technol. 19(5) (2010) 852–865 (2010). doi:10.1007/s11666-010-9492-1.

[32] E. Turunen, T. Varis, T.E. Gustafsson, J. Keskinen, T. Fält, S.P. Hannula, Parameter optimization of HVOF sprayed nanostructured alumina and alumina-nickel composite coatings, Surf. Coat. Technol. 200 (16–17) (2006) 4987–4994 (2006). doi:10.1016/j.surfcoat.2005.05.018. URL: https://linkinghub.elsevier.com/retrieve/pii/S0257897205006109.

[33] C. Lyphout, K. Sato, Screening design of hard metal feedstock powders for supersonic air fuel processing, Surf. Coat. Technol. 258 (2014) (2014) 447–457, https://doi.org/10.1016/j.surfcoat.2014.08.055.

[34] N. Pulido-González, S. García-Rodríguez, M. Campo, J. Rams, B. Torres, Application of DOE and ANOVA in Optimization of HVOF Spraying Parameters in the Development of New Ti Coatings, J. Therm. Spray Technol. 29(3) (2020) 384–399 (2020). doi:10.1007/s11666-020-00989-9.

[35] F. Yesildal, A.N. Ozakin, K. Yakut, Optimization of operational parameters for a photovoltaic panel cooled by spray cooling, Eng. Sci. Technol. 25 100983 (jan). doi:10.1016/J.JESTCH.2021.04.002. URL: https://linkinghub.elsevier.com/retrieve/pii/S2215098621000847.

[36] G.A. Clavijo-Mejía, D.G. Espinosa-Arbeláez, J.A. Hermann-Muñoz, A.L. Giraldo-Betancur, J. Muñoz-Saldaña, Effect of HVOF Process Parameters on TiO2 Coatings: An Approach Using DoE and First-Order Process Maps, J. Therm. Spray Technol. 28(6) (2019) 1160–1172 (2019). doi:10.1007/s11666-019-00895-9.

[37] M.N. Khan, S. Shah, T. Shamim, Investigation of operating parameters on high-velocity oxyfuel thermal spray coating quality for aerospace applications, Int. J. Adv. Manuf. Technol. 103 (5–8) (2019) 2677–2690 (2019). doi:10.1007/s00170-019-03696-0.

[38] K. Shivalingaiah, K.S. Sridhar, D. Sethuram, K.V. Murthy, P.G. Koppad, C.S. Ramesh, HVOF sprayed Inconel 718/cubic boron nitride composite coatings: Microstructure, microhardness and slurry erosive behaviour, Mater. Res. Express 6 (12) (2019) 1265i8 (feb 2019). doi:10.1088/2053-1591/ab7067.

[39] A. Amudha, H.S. Nagaraja, H.D. Shashikala, Mechanical and wetting properties of 25 spray technique, Physica B 602 (2021) 412409 (feb 2021). doi:10.1016/j.physb.2020.412409.

[40] J. Singh, S. Kumar, G. Singh, Taguchi's Approach for Optimization of Tribo-Resistance Parameters Forss304, in: Materials Today: Proceedings, Vol. 5, Elsevier Ltd, 2018, pp. 5031–5038 (2018). doi:10.1016/j.matpr.2017.12.081. URL: https://linkinghub.elsevier.com/retrieve/pii/S2214785317330602.

[41] T. Varis, T. Suhonen, O. Calonius, J. Čuban, M. Pietola, Optimization of HVOF Cr 3 C 2 NiCr coating for increased fatigue performance, Surf. Coat. Technol. 305 (2016) 123–131 (nov 2016). doi:10.1016/j.surfcoat.2016.08.012. URL: https://linkinghub.elsevier.com/retrieve/pii/S0257897216307368.

[42] X. Ran, J. Shang, L. Wang, X. Zhang, Effect of porosity on wear behaviour of remanufacturing Cr3C2-NiCr coatings under oil lubrication, in: Procedia Manufacturing, Vol. 43, Elsevier B.V., 2020, pp. 487–494 (2020). doi:10.1016/j.promfg.2020.02.184. URL: https://linkinghub.elsevier.com/retrieve/pii/S2351978920307708.

[43] A. Vats, A. Kumar, A. Patnaik, M.L. Meena, Influence of deposition parameters on Tribological Performance of HVOF Coating: A review, in: IOP Conference Series: Materials Science and Engineering, Vol. 1017, IOP Publishing Ltd, 2021, p. 12015 (2021). doi:10.1088/1757-899X/1017/1/012015.

[44] K. Padilla, A. Velásquez, J.A. Berríos, E.S.P. Cabrera, Fatigue behavior of a 4140 steel coated with a nimoal deposit applied by hvof thermal spray, Surface and Coatings Technology 150 (2002) 151–162 (2 2002). doi:10.1016/S0257-8972(01)01447-5.

[45] A.P. Krelling, M.M. de Souza, C.E. da Costa, J.C.G. Milan, Hvof-sprayed coating over aisi 4140 steel for hard chromium replacement, Mater. Res. 21 (2018), https://doi.org/10.1590/1980-5373-mr-2018-0138. URL: http://www.scielo.br/scielo.php?script=sci_arttext&pid=S1516-14392018000400225&lng=en&tlng=en.

[46] G. Bolelli, A. Colella, L. Lusvarghi, S. Morelli, P. Puddu, E. Righetti, P. Sassatelli, V. Testa, TiC–NiCr thermal spray coatings as an alternative to WC-CoCr and Cr3C2–NiCr, Wear 450–451 (March) (2020) 203273 (2020). doi:10.1016/j.wear.2020.203273.

[47] S. Thermsuk, P. Surin, Abrasion wear of HVOF sprayed coatings on SUS 400 stainless steel, Int. J. Appl. Eng. Res. 13 (20) (2018) 14675–14678.

[48] S. Hong, Y. Wu, Q. Wang, G. Ying, G. Li, W. Gao, B. Wang, W. Guo, Microstructure and cavitation-silt erosion behavior of high-velocity oxygen-

fuel (HVOF) sprayed Cr3C2-NiCr coating, Surf. Coat. Technol. 225 (2013) 85–91 (jun 2013). doi:10.1016/j.surfcoat.2013.03.020. URL: https://linkinghub.elsevier.com/retrieve/pii/S0257897213002727.

[49] D. Poirier, J.-G. Legoux, R.S. Lima, Engineering HVOF-Sprayed Cr3C2-NiCr Coatings: The Effect of Particle Morphology and Spraying Parameters on the Microstructure, Properties, and High Temperature Wear Performance, J. Therm. Spray Technol. 22 (2–3) (2013) 280–289 (mar 2013). doi:10.1007/s11666-012-9833-3.

[50] C. Li, X. Gao, D. Zhang, H. Gao, X. Han, B. Zhang, Numerical Investigation on the Flame Characteristics and Particle Behaviors in a HVOF Spray Process Using Kerosene as Fuel, J. Therm. Spray Technol. 30 (3) (2021) 725–738 (feb 2021). doi:10.1007/s11666-021-01165-3.

[51] A.G.M. Pukasiewicz, H.E. de Boer, G.B. Sucharski, R.F. Vaz, L.A.J. Procopiak, The influence of HVOF spraying parameters on the microstructure, residual stress and cavitation resistance of FeMnCrSi coatings, Surf. Coat. Technol. 327 (2017) 158–166 (oct 2017). doi:10.1016/j.surfcoat.2017.07.073. URL: https://linkinghub.elsevier.com/retrieve/pii/S0257897217307752.

[52] M. Abbas, G.M. Smith, P.R. Munroe, Microstructural study of HVOF sprayed Ni particles on a grit-blasted stainless-steel substrate, Surf. Coat. Technol. 409 (2021) 126832 (mar 2021). doi:10.1016/j.surfcoat.2021.126832. URL: https://linkinghub.elsevier.com/retrieve/pii/S025789722100005.

[53] M.A. Javed, A.S. Ang, C.M. Bhadra, R. Piola, W.C. Neil, C.C. Berndt, M. Leigh, H. Howse, S.A. Wade, Corrosion and mechanical performance of hvof wc-based coatings with alloyed nickel binder for use in marine hydraulic applications, Surf. Coat. Technol. 418 (2021) 127239 (7 2021). doi:10.1016/J.SURFCOAT.2021.127239.

[54] T. Sahraoui, N.E. Fenineche, G. Montavon, C. Coddet, Alternative to chromium: characteristics and wear behavior of hvof coatings for gas turbine shafts repair (heavy-duty), J. Mater. Process. Technol. 152 (2004) 43–55 (10 2004). doi:10.1016/J.JMATPROTEC.2004.02.061.

[55] H. Wu, X. Xie, M. Liu, C. Chen, H. Liao, Y. Zhang, S. Deng, A new approach to simulate coating thickness in cold spray, Surf. Coat. Technol. 382 (2020), https://doi.org/10.1016/j.surfcoat.2019.125151.

[56] C.A. Schneider, W.S. Rasband, K.W. Eliceiri, NIH Image to ImageJ: 25 years of image analysis, Nature Methods 9 (7) (2012) 671–675 (jul 2012). doi:10.1038/nmeth.2089. URL: https://www.nature.com/articles/nmeth.2089.

[57] Šárka Houdková, O. Bláhová, F. Zahálka, M. Kašparová, The instrumented indentation study of hvof-sprayed hardmetal coatings, J. Therm. Spray Technol. 21 (2012) 77–85 (2012). doi:10.1007/s11666-011-9677-2.

[58] X. Zhang, X.-B. Tian, Z.-W. Zhao, J.-B. Gao, Y.-W. Zhou, P. Gao, Y.-Y. Guo, Z. Lv, Evaluation of the adhesion and failure mechanism of the hard crn coatings on different substrates, Surf. Coat. Technol. 364 (2019) 135–143 (4 2019). doi:10.1016/j.surfcoat.2019.01.059. URL: https://linkinghub.elsevier.com/retrieve/pii/S0257897219300751.

[59] L. Qiao, Y. Wu, S. Hong, J. Zhang, W. Shi, Y. Zheng, Relationships between spray parameters, microstructures and ultrasonic cavitation erosion behavior of HVOF sprayed Fe-based amorphous/nanocrystalline coatings, Ultrason. Sonochem. 39 (2017) 39–46 (nov 2017). doi:10.1016/j.ultsonch.2017.04.011. URL: https://linkinghub.elsevier.com/retrieve/pii/S1350417717301694.

[60] B. Song, M. Bai, K.T. Voisey, T. Hussain, Role of Oxides and Porosity on High-Temperature Oxidation of Liquid-Fueled HVOF Thermal-Sprayed Ni50Cr Coatings, J. Therm. Spray Technol. 26 (3) (2017) 554–568 (feb 2017). doi:10.1007/s11666-017-0531-z.

[61] W. Tillmann, L. Hagen, C. Schaak, J. Liß, M. Schaper, K.P. Hoyer, M.E. Aydinöz, K. U. Garthe, Adhesion of HVOF-Sprayed WC-Co Coatings on 316L Substrates Processed by SLM, J. Therm. Spray Technol. 29 (6) (2020) 1396–1409 (2020). doi:10.1007/s11666-020-01081-y.

[62] R.S. Paredes, S.C. Amico, A.S. d'Oliveira, The effect of roughness and pre-heating of the substrate on the morphology of aluminium coatings deposited by thermal spraying, Surf. Coat. Technol. 200 (2006) 3049–3055 (2 2006). doi:10.1016/J.SURFCOAT.2005.02.200.

[63] A.W.Y. Tan, W. Sun, A. Bhowmik, J.Y. Lek, X. Song, W. Zhai, H. Zheng, F. Li, I. Marinescu, Z. Dong, E. Liu, Effect of substrate surface roughness on microstructure and mechanical properties of cold-sprayed ti6al4v coatings on ti6al4v substrates, J. Therm. Spray Technol. 28 (2019) 1959–1973 (12 2019). doi:10.1007/S11666-019-00926-5/FIGURES/14.

[64] R.P. Garcia, T. Luz, S.C. Canobre, al, Y. Cheng, S. Choi, T. Watanabe, B. Swain, A. Behera, Effect of powder feed rate on adhesion strength and microhardness of aps niti coating: a microstructural investigation, Surf. Topogr.: Metrol. Properties 9 (2021) 025039 (6 2021). doi:10.1088/2051-672X/AC0A38.